Supported Core@Shell Electrocatalysts for Fuel Cells: Close Encounter with Reality

Seung Jun Hwang[1], Sung Jong Yoo[1], Jungho Shin[2], Yong-Hun Cho[3], Jong Hyun Jang[1], Eunae Cho[1], Yung-Eun Sung[4], Suk Woo Nam[1], Tae-Hoon Lim[1], Seung-Cheol Lee[2] & Soo-Kil Kim[1,5]

[1]Fuel Cell Research Center, Korea Institute of Science and Technology, 39-1 Hawolgok-dong, Seoul 136-791, Korea, [2]Electronic Materials Research Center, Korea Institute of Science and Technology, 39-1 Hawolgok-dong, Seoul 136-791, Korea, [3]School of Advanced Materials Engineering, Kookmin University, 861-1 Jeongneung-dong, Seoul 136-702, Korea, [4]Center for Nanoparticle Research, Institute for Basic Science, School of Chemical and Biological Engineering, Seoul National University, 56-1 Shinlimdong, Seoul 151-742, Korea, [5]School of Integrative Engineering, Chung-Ang University, 221, Heukseok-Dong, Dongjak-Gu, Seoul, 156-756, Korea.

Core@shell electrocatalysts for fuel cells have the advantages of a high utilization of Pt and the modification of its electronic structures toward enhancement of the activities. In this study, we suggest both a theoretical background for the design of highly active and stable core@shell/C and a novel facile synthetic strategy for their preparation. Using density functional theory calculations guided by the oxygen adsorption energy and vacancy formation energy, $Pd_3Cu_1@Pt/C$ was selected as the most suitable candidate for the oxygen reduction reaction in terms of its activity and stability. These predictions were experimentally verified by the surfactant-free synthesis of Pd3Cu1/C cores and the selective Pt shell formation using a Hantzsch ester as a reducing agent. In a similar fashion, $Pd@Pd_4Ir_6/C$ catalyst was also designed and synthesized for the hydrogen oxidation reaction. The developed catalysts exhibited high activity, high selectivity, and 4,000 h of long-term durability at the single-cell level.

O ver the last few decades, advanced catalysts for low-temperature fuel cells have been extensively studied using theoretical design and experimental validation[1–5]. Nonetheless, there are still critical hurdles to overcome for electrocatalysis in proton exchange membrane fuel cells (PEMFCs), including 1) overcoming the sluggish oxygen reduction reaction (ORR) kinetics with a minimum amount of Pt, 2) developing novel selective catalysts for the hydrogen oxidation reaction (HOR) for the shutdown/startup stability of the stack, and 3) enhancing the physical/chemical durability of the catalysts[6–10]. Despite the synthetic challenges, several notable studies have found that non-noble metal-alloys had significant activity and durability.

The advantage of core@shell nanostructures is high Pt utilization by interposition of the non-noble core, which further alters the electronic structure of Pt and stabilizes it by enhancing the interfacial bonding between the core and shell[11]. To date, reports on core@shell ORR catalysts can be classified by their synthetic approaches, which include the seed mediated sequential method[12,13], the galvanic-replacement reaction[14,15], and structural rearrangement (de-alloying or segregation)[16–19]. However, studies of well-defined multi-metallic core@shells smaller than 10 nm are rare, particularly for the supported form that exhibits significant activity and durability and can potentially be used in real cells.

In this study, we computationally screened the potential core@shell combination and devised a facile synthesis route for the proposed structures. We also characterized performance and durability at the single cell level. To determine the best core@shell combinations for ORR, we performed density functional theory (DFT) calculations using two descriptors. The first descriptor is the oxygen adsorption energy (OAE) on the Pt shell to measure the reactivity[10,20]. The other descriptor is the vacancy formation energy (VFE) of Pt in the Pt shell to measure stability proposed in this study.

Results

The computational screening of activity and durability was performed on the overlayer-substrate system, which mimics core@shells, to avoid the complexity introduced from multiple atoms in the particles. In order to screen as many core@shell systems as possible, the thickness of the Pt overlayer was fixed at 1 monolayer (ML) (see

Supplementary Fig. S24, S25 for details). The OAEs and VFEs of the pure elemental cores (Pd, Ir, Ni) are presented as open squares in Fig. 1. The ΔOAE on vertical scale is difference between bulk Pt and core@shell structured model catalysts. The optimum ΔOAE value (the horizontal dashed line) was referred from the work by Nørskov et al.[20] and Greeley et al.[10]. The VFEs on the horizontal scale are the averages which represent mixed property for symetically two distinct sites of "Up" and "Down" (Fig. S25). The OAEs of some metal@Pt were predicted to have better reactivity or stability than pure Pt. However, the reactivity was still far from the optimum value (the horizontal dashed line), which prompted us to extend the combinations to alloy cores (black circles). Though Pt_3Ni_1@Pt was predicted to be the most reactive, it was excluded due to its poor stability (i.e., its VFE was the lowest in alloy cores), which would result in poor long-term operational performance. Pt_3Ni_1@Pt and Pd_3Fe_1@Pt were predicted to have weaker OAE and corresponded to the experemental results[6,21]. The better activity of Pt_3Ni_1@Pt reported from experiment could be explained by fact that the OAE of Pt_3Ni_1@Pt is closer to the optimum value than that of Pt. However, for Pd_3Fe_1@Pt, calculation showed a slight disagreement with experiment[21]; the stronger OAE and better activity than that of the calculation. According to the experiment the activity of Pd_3Fe_1@Pt was several times higher than that of Pt. This discrepancy might be originated from the uncertainty in the optimum value or computational accuracy. However, based on the relatively good stability and reactivity of Pd@Pt, we focused our attention on Pd-based 3d transition metal alloy cores to minimize the cost/activity ratio. As shown in Fig. 1, Pd_3Cu_1@Pt has the most suitable OAE and VFE, implying significant activity and durability. In addition, we devised a facile and robust route to synthesize this core@shell[22,23].

Our novel two-step synthetic method is illustrated in Fig. 2. For the production of the C-supported form, the shell generation is typically achieved by reduction of the precursor on the prepared cores/C using a mild reducing reagent with the proper surfactants[24-27], which can result in the simultaneous reduction of the precursor on the cores and carbon. This problem can be avoided by adding carbon in the final stage. However, this method still suffers from a weak metal-support interaction, an inability to precisely control the metal loading, and the need for additional treatment. Thus, selective reduction of the Pt shell on the core would be highly beneficial.

The preparation of a monodispersed core/C is a prerequisite for the uniform reduction of the shell because the reduction potential of the shell precursor varies with the core size[28]. Although strong binding surfactants (i.e., amine reagents containing long alkyl chains and phosphine ligands) have traditionally been employed to synthesize the monodispersed metal nanoparticles, their residues may deteriorate the activities of the nanoparticles. Thus, understanding the surface chemistry of colloidal nanoparticles is crucial for developing an efficient stabilizing system. We postulated that benzyl ether could be utilized as a solvent and weak coordinating surfactant for the synthesis of Pd-based cores. Its short alkyl chain and weak coordinating property compared to nitrogen or phosphorous eliminates the need for its removal by unwanted heat treatment. Based on these characteristics, the synthesis of Pd/C and Pd_3Cu_1/C has been accomplished using benzyl ether and a mild borane tert-butylamine complex as a reducing reagent. A TEM image showed that Pd/C and Pd_3Cu_1/C are mono-dispersed with particle sizes of 3.5 nm (Fig. 3a and 3b). The lattice distances of Pd (2.41 Å) and Pd_3Cu_1 (2.12 Å), which were also analyzed by HRTEM, corresponded well with the XRD data (Supplementary Fig. S8–S12).

Adzic showed examples of Pd@Pt or PdAu@Pt electrocatalysts using galvanic displacement with sacrificing Cu[29]. Though the displacement enabled the preferential deposition of Pt on the cores, the retention of Cu as an alloy core material may be difficult with their method. We have tried to find mild redox systems that are capable of reducing the precursor on the metal surface but not strong enough to reduce the precursor on the carbon. A naturally occurring hydrogenation redox process[30] involving a combination of enzymes and hydride reduction cofactors is a good example. The Hantzsch ester, which was developed to perform the highly enantioselective transfer hydrogenation in organometallic chemistry[31], is a suitable reducing agent for the preferential deposition of the shell on the cores. To the best of our knowledge, this is the first study that uses the Hantzsch ester as a reducing agent for the synthesis of inorganic nanoparticles.

The TEM micrographs (Fig. 3c and 3d) show well-dispersed spherical Pd_3Cu_1@Pt/C and $Pd@Pd_4Ir_6$/C particles that are larger than the cores (5 nm for Pd_3Cu_1@Pt and 8 nm for $Pd@Pd_4Ir_6$). It should be noted that isolated Pt or Pd_4Ir_6 nanoparticles were not found on the carbon, implying the exclusive deposition of the shell material on the cores. Although Cu loss due to displacement with the Pt precursor occurred in the absence of the Hantzsch ester, no such loss occurred in its presence. The unique function of the Hantzsch ester was further verified by the failure to form a selective shell in the presence of ascorbic acid or sodium borohydride, which are common reducing agents for core@shell synthesis (Supplementary Fig. S5, S6). Figure 3e,f depict the line-profile analysis using aberration-corrected STEM/energy dispersive spectrometry (EDS), revealing the distribution of the components in $Pd@Pd_4Ir_6$/C and Pd_3Cu_1@Pt/C. The lower Ir and Pt intensities and higher Pd and Cu intensities at the center clearly verify the formation of core@shell structures. The shell thicknesses and composition/amounts of the core were easily controlled (note that the shell thickness of Pd_3Cu_1@Pt was approximately 1 nm; 2−3 monolayers of Pt).

We performed an in-depth analysis by powder X-ray diffraction (PXRD) and extended X-ray absorption fine structure (EXAFS) studies to characterize the structure of the core@shell. Supplementary Figure S12 shows the PXRD scans, in which the Pd (111) of Pd_3Cu_1/C shifted to higher angles than that of pure Pd/C, indicating lattice contraction due to alloy formation. The contribution of Pt became clear after coating the Pt shell on the Pd_3Cu_1/C, which again shifted the peak to lower angles. This re-shifting indicates that the preparation of the Pt atoms on the Pd_3Cu_1 surface was satisfactory (note that Pt (111) exhibits an angle that is 0.356 degrees lower than that of Pd (111)). The local structural information of Pd_3Cu_1@Pt, such as the geometric effect of the Pd_3Cu_1 substrate on the contraction of the Pt shell due to variations in the shell thickness and Pt–Pt coordination number (CN), was obtained by Fourier-transformed (FT) k3-weighed EXAFS analysis at the Pt L_{III} edge (Fig. S16). The peak centered at 2.5 Å represents the contribution of the first
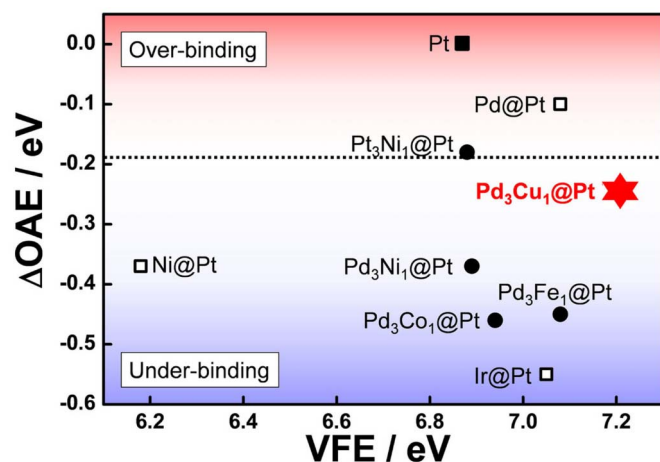

Figure 1 | The computational screening of Pt-coated suitable core materials for the high activity and durability. The calculation was performed on the overlayer-substrate system with the fixed thickness of the Pt overlayer (1 monolayer). The optimum value of the reactivity indicated in the horizontal dashed line.
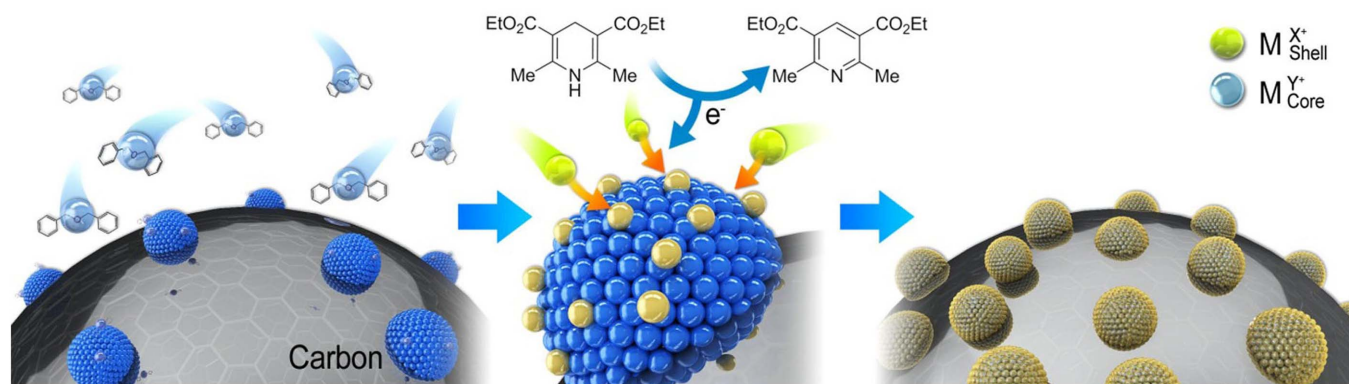
Figure 2 | Illustration of our novel two-step synthetic schemes for core@shell catalysts. Benzyl ether was utilized as a solvent as well as a weak coordinating surfactant for the synthesis of Pd-based cores without using surfactants. The Hantzsch ester is capable of reducing the shell precursors selectively on the core surface.

metal-metal coordination shell to the EXAFS oscillations. It is interesting to note that the FT features of the core@shells with various shell thicknesses exhibited different oscillation patterns compared to commercial Pt/C (Johnson Matthey, JM), indicating the different Pt phase structures (Supplementary Fig. S16). In addition, Supplementary Table S1 clearly shows the structural difference between the core@shells and commercial Pt/C. The lower Pt–Pt CN (3.0) of Pd_3Cu_1@Pt with a 0.7 eq Pt implies a Pt shell structure because such a configuration causes the Pt environment to be less coordinated by its metallic neighbors due to surface truncation effects[32,33] (note that the CN of JM Pt/C is 6.6). The Pt–Pt CN increased and the Pt–Pd and Pt–Cu CNs decreased as the Pt shell thickness increased, which provides additional evidence for the covering of the Pd_3Cu_1 core with a Pt shell (Supplementary Table S1). The cyclic voltammogram (CV) in an O_2-free electrolyte can provide further evidence. For example, a distinctive sharp Ir peak[34] was observed when the Pd_4Ir_6 layer was coated on the Pd/C surface of Pd@Pd_4Ir_6/C (Supplementary Fig. S20). Pt- and PdIr-coated core@shells, which have a larger electrochemically active surface area than the cores and exhibit the dominant characteristics of Pt and PdIr, reflect the formation of core@shells. Thus, the STEM, XRD, EXAFS, and CV results strongly support the formation of core@shell structures.

Figure 4a summarizes the ORR kinetics of the different alloys, core@shells, and JM 40 wt% Pt/C catalysts. The JM Pt/C catalyst has a particle size of 2–5 nm with a most probable size of 3 nm. The half-wave potential (HWP) exhibits the following trend: Pd_3Cu_1@Pt/C > JM Pt/C > Pd_3Cu_1/C > Pd/C > Pd@Pd_4Ir_6/C. The kinetic current density of 0.9 V vs. RHE for Pd_3Cu_1@Pt/C was also much higher than that of the JM Pt/C. For a more detailed understanding, the ORR kinetics as a function of shell thickness were compared (Supplementary Fig. S17). The Pt-mass-normalized current density of Pd_3Cu_1@Pt with a 0.7 eq Pt shell content was 2.6 times higher than that of JM Pt/C. In addition, the current density of the smaller Pt shell content (0.7 eq) was 1.7 times higher than that of the 1.5 eq Pt shell, which corresponds to a shell that is 1.8 times thicker, and the smaller Pt shell had a more positive HWP (by 15 mV); these results indicate the dependency of Pd_3Cu_1@Pt activity on the thickness of the Pt shell. A similar effect was achieved by tuning the core size (Supplementary Fig. S18). For example, Pd_3Cu_1@Pt with a 45% Pd_3Cu_1/C core exhibited a 40-mV positive shift in the HWP compared to that of the 30% core. The increase in the loading amounts from 30 to 45% is equivalent to increase in the core size by around 0.5 nm.

Another interesting result is that while the Pt shell coating on Pd_3Cu_1 greatly enhanced the ORR activity, the Pd_4Ir_6 shell coating on Pd deteriorated it, leading to an inactive ORR. However, the

Pd@Pd_4Ir_6/C exhibited high activity for HOR, as shown in Fig. 4b. The comparison of the mass-transfer-corrected Tafel plots and exchange current densities clearly showed that Pd@Ir_6/C displayed a higher activity for HOR than JM Pt/C. The significance of this result in combination with the results in Fig. 4a can be summarized as follows: i) a consolidated synthetic method for making highly active catalysts for both electrodes, ii) the possibility of a highly active Pt-free anode catalyst, and iii) the potential for a HOR-selective catalyst that prevents carbon corrosion during the startup/shutdown processes[35,36]. Markovic et al. have suggested a chemical modification of the anode catalyst that would suppress the ORR[8,37]. However, our research suggests that the selectivity of the catalysts for ORR and HOR can easily be controlled by tuning the core@shell metals and fine-tuning the core size and shell thickness with our simple and novel synthetic method.

The single cell performances for both Pd_3Cu_1@Pt/C and JM Pt/C as cathode catalysts (0.3 mg_{metal}/cm^2) are shown in Fig. 4c under the following operation conditions: 10 cm^2 active area, 70°C, and atmospheric pressure. The MEA with Pd_3Cu_1@Pt/C catalysts exhibited the best performance in the range of >0.5 V, particularly in the high voltage area (0.9–0.6 V), where the currents were 1.6 and 2.0 times higher than those of Pt/C MEA at 0.7 V and 0.8 V, respectively. The mass activities (inset) were also compared in terms of Pt mass and Pt + Pd mass and showed a higher mass activity for Pd_3Cu_1@Pt/C even when based on the Pt + Pd mass. The stability test of the Pd_3Cu_1@Pt/C single cell was performed at 400 mA/cm^2 (Fig. 4d) and resulted in an approximately 8% (0.73 V to 0.67 V) decay rate, even after 4,000 h of operation. The inset of Fig. 4d provides the results of the accelerated stability tests with potential cycling between open circuit voltage to 0.35 V and a scan rate of 10 mA/cm^2·sec at 70°C. After 3,000 min of potential cycling, the Pt/C cell performance decreased to 65% and 45% of its initial performance at 0.6 V and 0.7 V, respectively. However, the degradation of the Pd_3Cu_1@Pt/C single cell was half of the Pt/C cell degradation, indicating the superior stability of Pd_3Cu_1@Pt/C.

The OAEs with various Pt thickness for Pd_3Cu_1@Pt/C were presented in Fig. S27 (b). The OAE for Pt 2 ML showed the closest value to the optimum and corresponded well to experimental results for 2 ML of Pt covered the Pd_3Cu core. However, from the veiwpoint of durably, Pt 1 ML showed the largest VFE as shown in Fig. S27 (a). This enhanced durability for Pt 1 ML were investigated using a Bader analysis of Pd_3Cu_1@Pt/C with Pt 1 ML compared to pure Pt layers (table S2). For pure Pt, there was a slight charge transfer from the subsurface to the surface by Friedel oscillations. The total charge at the surface Pt was estimated to be 10.045. The Bader charges of Pd and Cu in the bulk Pd_3Cu phase are 10.10 and 10.70, respectively, implying a transfer of 0.1 electron from Cu to Pd. There was a
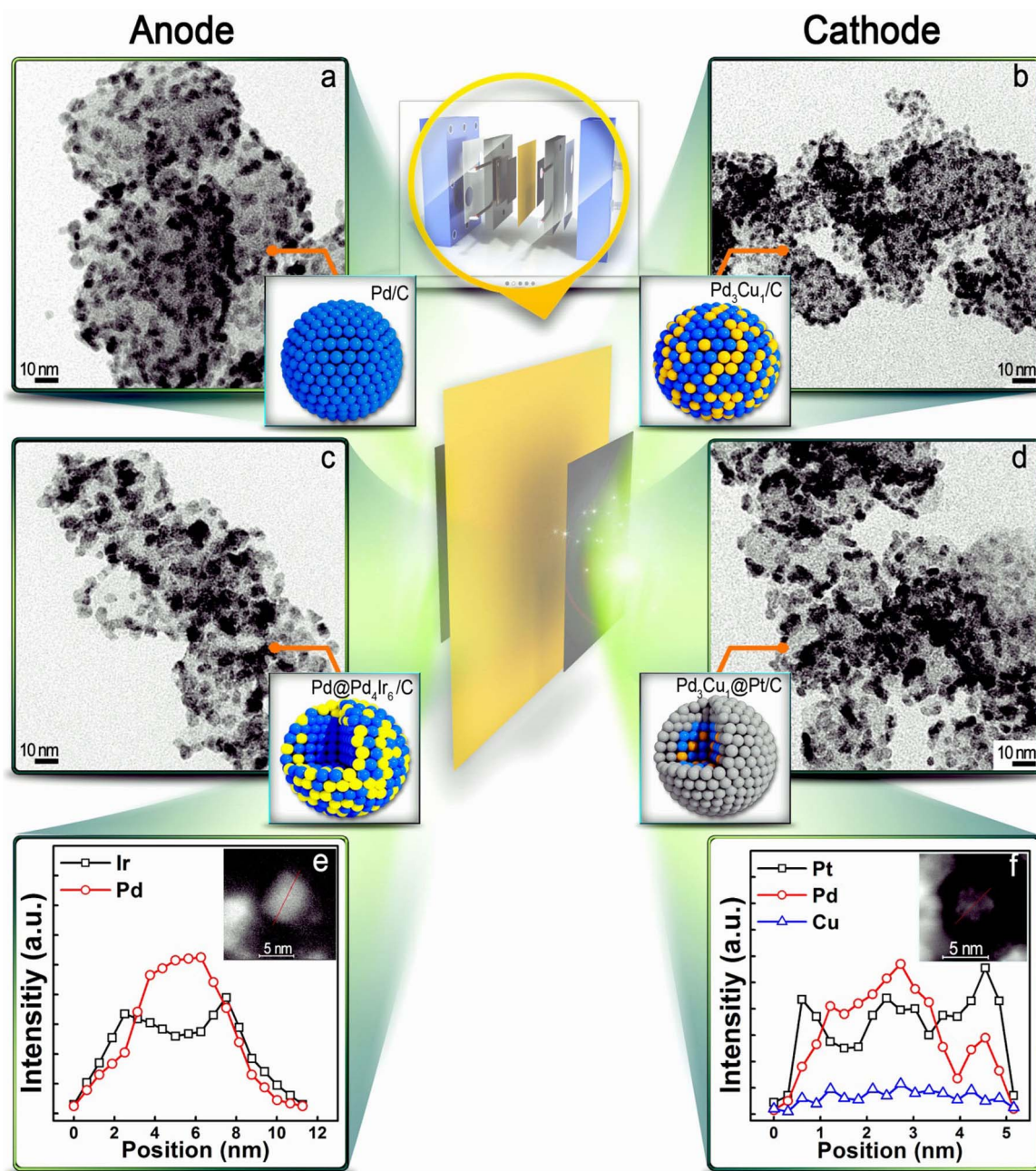
Figure 3 | TEM images of carbon-supported core and core@shell nanoparticles (NPs). (a), Pd/C NPs synthesized with borane *tert*-butylamine complex in benzyl ether. (b), Pd_3Cu_1/C NPs prepared in the same manner. (c), $Pd@P_4Ir_6$/C and (d), $Pd_3Cu_1@Pt$/C core@shell electrocatalysts. HAADF-STEM images and their line profiles: (e), $Pd@P_4Ir_6$ and (f), $Pd_3Cu_1@Pt$.

significant charge transfer from Pd_3Cu to Pt (Table S2; 0.112 electron from Pd, and 0.06 electron from Cu). Because Pd had already gained electrons from Cu, it had a sufficient amount of potential to transfer electrons to Pt. In addition, Cu was expected to exhibit a small amount of charge transfer[38]. By increasing the Pt thickness to more than 2 ML, the charge at the surface Pt atom approached the value of pure Pt (10.045), which predicted the same VFEs for Pt layers thicker than 2 ML.

In addition, the electron donation from the Pd_3Cu_1 sub-layer to Pt was verified by the X-ray absorption near-edge structure (XANES) on the Pt L_{III} edges of $Pd_3Cu_1@Pt$/C by varying the Pt thickness (Fig. 5a). The Pt *d*-band vacancy from the Pt L_{III} white lines verified the electron transfer between the core and shell. It is important to note that the intensity of the white line, the magnitude of which is a

direct measure of *d*-band vacancies, decreases as the Pt shell thickness decreases. Based on the studies by other researchers[39] and our previous study[40], these XANES data clearly indicate electron donation from the Pd_3Cu_1 to Pt through strong metal-metal interactions[41].

For more a precise understanding of the electronic origin, we plotted the OAEs as a function of the local density of state (LDOS) at the Fermi level, as shown in Supplementary Fig. S28. As with the previous results[42], a linear relationship was observed, which indicated that the LDOS at the Fermi level was a good descriptor for predicting ORR activity. For predicting the stability, we plotted the difference in the charge density of $Pd_3Cu_1@Pt$ from its pure states of Pd_3Cu_1 and Pt (Fig. 5b). Charge accumulation (yellow) along the Pt and Pd_3Cu_1 interface was obtained, while charge dissipation was found in the
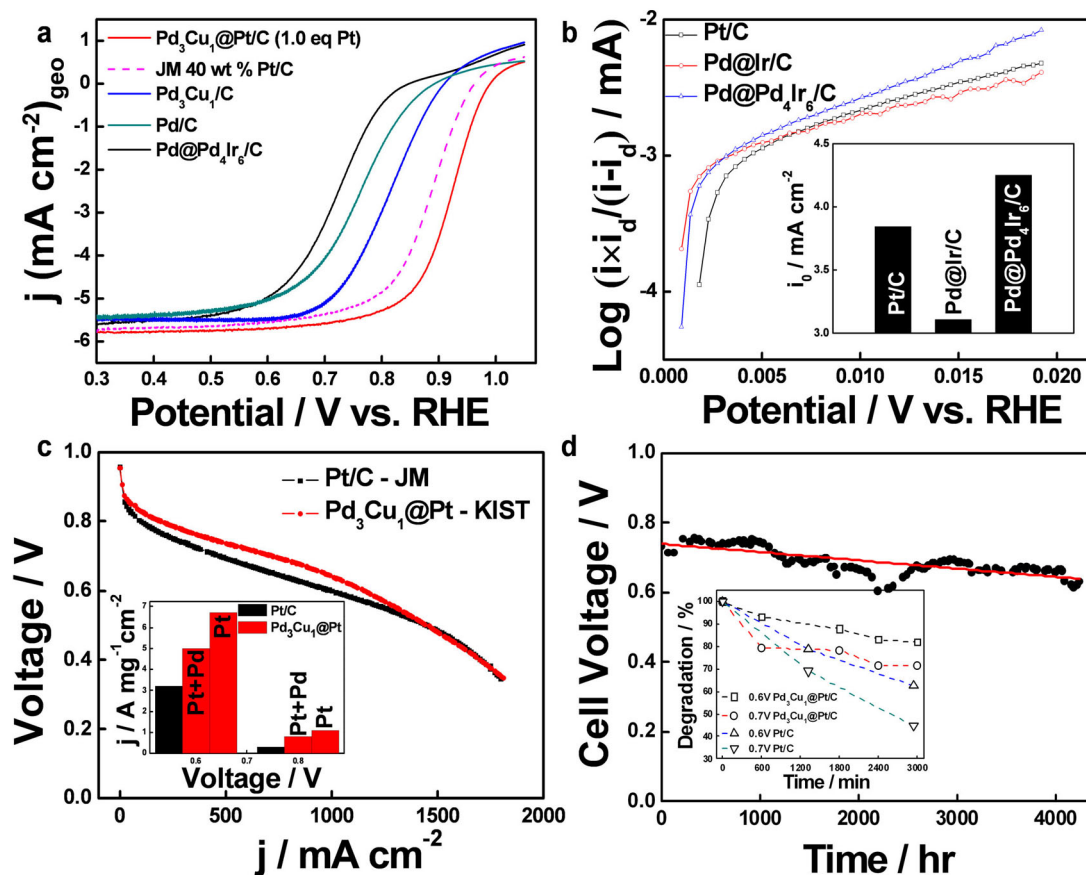
Figure 4 | ORR and HOR performance of carbon-supported core@shell catalysts in half-cell and their single cell performance and stability. a, ORR polarization curves for the Pd/C, Pd_3Cu_1/C, Pd_3Cu_1@Pt/C, Pd@Pd_4Ir_6/C, and Pt/C (room temperature, O_2-saturated 0.1 M $HClO_4$ solution, 10 mV/s, 1600 rpm). b, Tafel plot and the exchange current density (inset) for hydrogen oxidation reaction on Pt/C, Pd@Ir/C, and Pd@PdIr/C (H_2-saturated 0.5 M H_2SO_4 solution, 276 K, 20 mV/s, 1000 to 3000 rpm). c, The single cell polarization curves for both Pd_3Cu_1@Pt/C and JM Pt/C as cathode catalysts (0.3 mg_{metal}/cm^2, 10 cm^2 active area, 70°C, atmospheric pressure). Inset: mass activities in terms of Pt mass and Pt + Pd mass. d, The stability test of the Pd_3Cu_1@Pt/C single cell (400 mA/cm^2, air-interruption method). Inset: the accelerated stability tests with potential cycling (OCP to 0.35 V, 10 mA/cm^2·sec, 70°C).

Pd_3Cu_1 substrate, implying charge transfer from the substrate to the Pt overlayer (Fig. 5c). The distribution of the transferred charge from Pd_3Cu_1 differs from other Pt_3M systems. Compared to the triangular-shaped charge transfer for other Pt_3M systems (Supplementary Fig. S29), the transferred charge in the Pd_3Cu_1 system forms a hexagonal ring consisting of three Pd and three Pt atoms (Fig. 5b), indicating that the active material for the charge transfer and interfacial bonding of Pd_3Cu_1@Pt was Pd.

Discussion

We have designed and developed highly active and stable Pd_3Cu_1@Pt/C (ORR) and Pd@PdIr (HOR) electrocatalysts. The new core@shell combinations were designed using DFT calculations guided by the OAE and VFE. First, the surfactant-free synthesis of core/C and the subsequent exclusive shell formations on the core using the Hantzsch ester as a reducing agent were demonstrated for the first time. Superior characteristics, such as high activity, HOR selectivity, and 4,000 h of long-term durability, were achieved with the novel core@shell/C catalysts. The DFT calculations and XANES analysis strongly support the origin of the enhanced characteristics. The descriptors used in this study can be extended to screen other core@shell combinations.

Methods

Chemical and materials. Dihydrogen hexachloroplatinate (IV) hexahydrate, (H_2PtCl_6·$6H_2O$, 99.9%) was purchased from Alfa Aesar. Palladium (II)

acetylacetonate (Pd($C_5H_8O_2$)$_2$, 99%), Copper (II) acetylacetonate (Cu($C_5H_8O_2$)$_2$, $\geq$ 99.99%), Iridium (III) chloride hydrate ($IrCl_3$·H_2O, $\geq$ 99.9%), Borane *tert*-butylamine complex ($C_4H_{14}BN$, 97%), benzyl ether ($C_{14}H_{14}O$, 98%), 200 proof anhydrous ethanol (C_2H_6O, $\geq$ 99.5%), and perchloric acid ($HClO_4$, 70%) were purchased from Aldrich. Diethyl 1,4-dihydro-2,6-dimethyl-3,5-pyridinedicarboxylate ($C_{13}H_{19}NO_4$, Hantzsch ester) was purchased from TCI. Unless otherwise stated, all commercial reagents and solvents were used without additional purification.

Synthesis of carbon-supported Pd electrocatalysts (30 wt % of Pd/C). To a three-neck round bottle flask (250 mL), carbon black (Vulcan XC-72R, 0.10 g) was dispersed in the 40 mL of benzyl ether, and stirred for 10 min at room temperature. Pd(acac)$_2$ (121.9 mg, 0.40 mmol) dissolved in benzyl ether (40 mL) were added to the reaction mixture at 70°C, followed by the addtion of the solution, borane *tert*-butylamine complex (97%, 600 mg) in 20 mL of benzyl ether. The resulting mixture was sealed with a Teflon and stirred at 100°C for 4 h under Ar atmosphere. The reaction was cooled to room temperature, filtered through washing with pure ethanol (J.T. Baker, 99.0%). The filtered pastes were dried in the vacuum oven at 40°C for 4 h. Pd_3Cu_1/C core nanoparticles were prepared in the same manner as described above, except that 119.4 mg of Pd(acac)$_2$ and 34.2 mg of Cu(acac)$_2$ were used as the precursors of the metal for forming core materials.

Shell deposition on carbon-supported core nanoparticles using Hantzsch ester. Pt and Pd_4Ir_6 shell layer on the surface of the core nanoparticles follows the same procedure as that for both Pd_3Cu_1/C and Pd/C. For the formation of Pt or PdIr shell electrocatalysts, 50 mg of Pd_3Cu_1/C or Pd/C was dispersed in 150 mL of anhydrous ethanol and sonicated for 30 seconds. Dihydrogen hexachloroplatinate (IV) hexahydrate, (H_2PtCl_6·$6H_2O$, 124.3 mg, 1.5 eq) and Hantzsch ester (5 eq of a Pt precursor, 1.2 mmol) dissolved in 40 and 20 mL of anhydrous ethanol respectively were added to the reaction solution at room temperature. (In the case of Pd_4Ir_6 shell, K_2PdCl_4 and $IrCl_3$·H_2O were used as precursors). The reaction mixture was then heated to 80°C. Once the temperature of the reaction mixture reached 80°C, the solution was additionally stirred 2 h under Ar atmosphere. The reaction was cooled
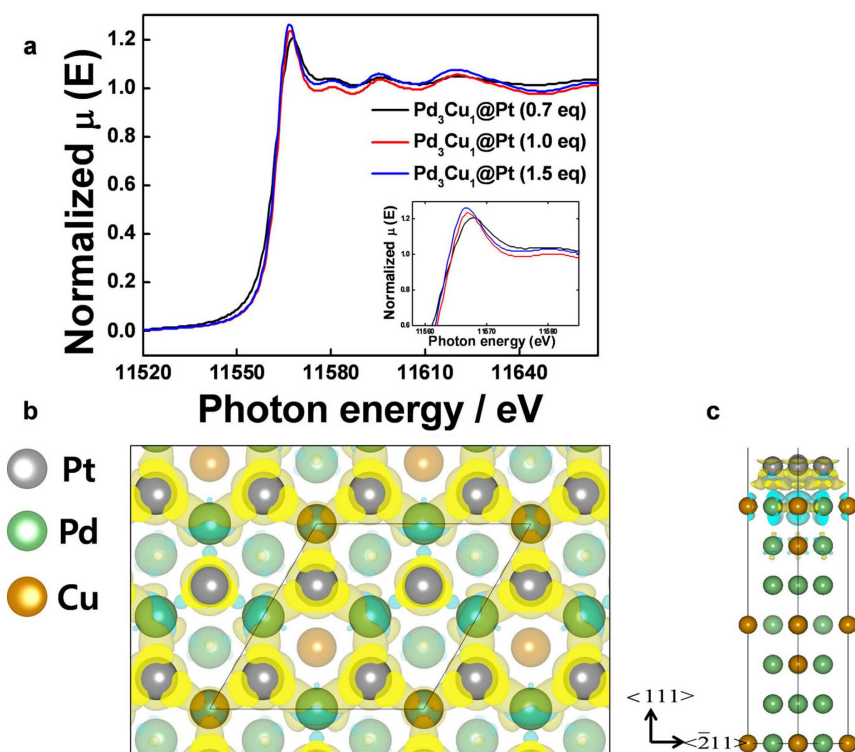
Figure 5 | Analysis and simulation of electronic structure in carbon-supported core@shell catalysts. (a), Pt L_{III}-edge XANES spectra and variation in unfilled *d*-states for samples having different shell thickness. Inset: enlargement of Pt L_{III}-edge XANES white line. (b), The distribution of the transferred charge from Pd_3Cu_1 in comparison with other Pt_3M (M = Ni, Co, Fe). (c), Charge accumulation (yellow) along the Pt and Pd_3Cu_1 interface and charge dissipation (cyan) in the Pd_3Cu_1 substrate.

to room temperature, filtered through washing with pure ethanol (J.T. Baker, 99.0%). The filtered pastes were dried in the vacuum oven at 40°C for 4 h.

Characterization. Prepared Pd/C, Pd_3Cu_1/C, Pd_3Cu_1@Pt/C, and $Pd@Pd_4Ir_6$/C electrocatalysts were examined by X-ray diffraction (XRD, Rigaku D/Max 2500) with Cu Kα radiation, and X-ray photoelectron spectra (XPS, PHI 5800 ESCA) were obtained from a monochromator (Al Kα source) calibrated with respect to the C (1s) peak at 284.6 eV. EXAFS and XANES were conducted at the Pohang Light Source (PLS) with a ring current of 120–170 mA at 2.5 GeV using the 5A1 beamline. Particle size, size distribution, dispersion were confirmed by transmission electron microscopy (TEM, Philips CM30) and high resolution transmission electron microscopy (HR-TEM, FEI, 200 keV). The core@shell structure and chemical distribution of Pd_3Cu_1@Pt/C and $Pd@Pd_4Ir_6$/C nanoparticles were examined using an aberration-corrected 200 keV scanning transmission electron microscope (STEM) (Titan, FEI).

1. Gasteiger, H. A. & Markovic, N. M. Just a Dream—or Future Reality? *Science* **324**, 48–49 (2009).
2. Lim, B. *et al*. Pd-Pt Bimetallic Nanodendrites with High Activity for Oxygen Reduction. *Science* **324**, 1302–1305 (2009).
3. Nørskov, J. K. & Christensen, C. H. Toward Efficient Hydrogen Production at Surfaces. *Science* **312**, 1322–1323 (2006).
4. Nørskov, J. K., Bligaard, T., Rossmeisl, J. & Christensen, C. H. Towards the computational design of solid catalysts. *Nat. Chem.* **1**, 37–46 (2009).
5. Liang, Y. *et al*. Co₃O₄ nanocrystals on graphene as a synergistic catalyst for oxygen reduction reaction. *Nat. Mater.* **10**, 780–786 (2011).
6. Stamenkovic, V. R. *et al*. Improved Oxygen Reduction Activity on Pt₃Ni(111) via Increased Surface Site Availability. *Science* **315**, 493–497 (2007).
7. Stamenkovic, V. R. *et al*. Trends in electrocatalysis on extended and nanoscale Pt-bimetallic alloy surfaces *Nat. Mater.* **6**, 241–247 (2007).
8. Genorio, B. *et al*. Selective catalysts for the hydrogen oxidation and oxygen reduction reactions by patterning of platinum with calix[4]arene molecules. *Nat. Mater.* **9**, 998–1003 (2010).
9. Zhang, J., Sasaki, K., Sutter, E. & Adzic, R. R. Stabilization of Platinum Oxygen-Reduction Electrocatalysts Using Gold Clusters. *Science* **315**, 220–222 (2007).
10. Greeley, J. *et al*. Alloys of platinum and early transition metals as oxygen reduction electrocatalysts. *Nat. Mater.* **1**, 552–556 (2009).
11. Yang, H. Platinum-Based Electrocatalysts with Core–Shell Nanostructures. *Angew. Chem. Int. Ed.* **50**, 2674–2676 (2011).
12. Mazumder, V., Chi, M., More, K. L. & Sun, S. Synthesis and Characterization of Multimetallic Pd/Au and Pd/Au/FePt Core/Shell Nanoparticles. *Angew. Chem. Int. Ed.* **49**, 9368–9372 (2010).
13. Mazumder, V., Chi, M., More, K. L. & Sun, S. Core/Shell Pd/FePt Nanoparticles as an Active and Durable Catalyst for the Oxygen Reduction Reaction. *J. Am. Chem. Soc.* **132**, 7848–7849 (2010).
14. Wang, J. X. *et al*. Oxygen Reduction on Well-Defined Core-Shell Nanocatalysts: Particle Size, Facet, and Pt Shell Thickness Effects. *J. Am. Chem. Soc.* **131**, 17298–17302 (2009).
15. Gong, K., Su, D. & Adzic, R. R. Platinum-Monolayer Shell on AuNi₀.₅Fe Nanoparticle Core Electrocatalyst with High Activity and Stability for the Oxygen Reduction Reaction. *J. Am. Chem. Soc.* **132**, 14364–14366 (2010).
16. Mayrhofer, K. J. J., Juhart, V., Hartl, K., Hanzlik, M. & Zrenz, M. Adsorbate-Induced Surface Segregation for Core–Shell Nanocatalysts. *Angew. Chem. Int. Ed.* **48**, 3529–3531 (2009).
17. Koh, S. & Strasser, P. Electrocatalysis on Bimetallic Surfaces: Modifying Catalytic Reactivity for Oxygen Reduction by Voltammetric Surface Dealloying. *J. Am. Chem. Soc.* **129**, 12624–12625 (2007).
18. Chen, S. *et al*. Enhanced Activity for Oxygen Reduction Reaction on "Pt₃Co" Nanoparticles: Direct Evidence of Percolated and Sandwich-Segregation Structures. *J. Am. Chem. Soc.* **130**, 13818–13819 (2008).
19. Strasser, P. *et al*. Lattice-strain control of the activity in dealloyed core–shell fuel cell catalysts. *Nat. Chem.* **2**, 454–460 (2010).
20. Norskov, J. K. *et al*. Origin of the overpotential for oxygen reduction at a fuel-cell cathode. *J. Phys. Chem. B* **108**, 17886–17892 (2004).
21. Shao, M. H. *et al*. Pd₃Fe and Pt Monolayer-Modified Pd₃Fe Electrocatalyst for Oxygen Reduction. *Z. Phys. Chem* **221**, 1175–1190 (2007).
22. Shao, M., Shoemaker, K., Peles, A., Kaneko, K. & Protsailo, L. Pt Monolayer on Porous Pd−Cu Alloys as Oxygen Reduction Electrocatalysts. *J. Am. Chem. Soc.* **132**, 9253–9255 (2010).
23. Stephens, I. E. L. *et al*. Tuning the Activity of Pt(111) for Oxygen Electroreduction by Subsurface Alloying. *J. Am. Chem. Soc.* **133**, 5485–5491 (2011).
24. Schmid, G., Lehnert, A., Malm, J. O. & Bovin, J. O. Ligand-Stabilized Bimetallic Colloids Identified by HRTEM and EDX. *Angew. Chem. Int. Ed.* **30**, 874–876 (1991).
25. Wang, Y. & Toshima, N. Preparation of Pd-Pt bimetallic colloids with controllable core/shell structures. *J. Phys. Chem. B* **101**, 5301–5306 (1997).
26. Habas, S. E., Lee, H., Radmilovic, V., Somorjai, G. A. & Yang, P. Shaping binary metal nanocrystals through epitaxial seeded growth. *Nat. Mater.* **6**, 692–697 (2007).
27. LaMer, V. K. & Dinegar, R. H. Theory, Production and Mechanism of Formation of Monodispersed Hydrosols. *J. Am. Chem. Soc.* **72**, 4847–4854 (1950).

28. Plieth, W. J. Electrochemical Properties of Small Clusters of Metal Atoms and Their Role in Surface Enhanced Raman-Scattering. *J. Phys. Chem.* **86**, 3166–3170 (1982).

29. Sasaki, K. *et al*. Core-Protected Platinum Monolayer Shell High-Stability Electrocatalysts for Fuel-Cell Cathodes. *Angew. Chem. Int. Ed.* **49**, 8602–8607 (2010).

30. Perrault, S. D. & Chan, W. C. W. Synthesis and Surface Modification of Highly Monodispersed, Spherical Gold Nanoparticles of 50–200 nm. *J. Am. Chem. Soc.* **131**, 17042–17043 (2009).

31. Ouellet, S. G., Walji, A. M. & Macmillan, D. W. C. Enantioselective Organocatalytic Transfer Hydrogenation Reactions using Hantzsch Esters. *Acc. Chem. Res.* **40**, 1327–1339 (2007).

32. Du, W. *et al*. Highly Active Iridium/Iridium-Tin/Tin Oxide Heterogeneous Nanoparticles as Alternative Electrocatalysts for the Ethanol Oxidation Reaction. *J. Am. Chem. Soc.* **133**, 15172–15183 (2011).

33. Frenkel, A. Z. Solving the 3D structure of metal nanoparticles. *Kristallogr.* **222**, 605–611 (2007).

34. Reier, T., Oezaslan, M. & Strasser, P. Electrocatalytic Oxygen Evolution (OER) on Ru, Ir, and Pt Catalysts: A Comparative Study of Nanoparticles and Bulk Materials. *ACS Catal.* **2**, 1756–1772 (2012).

35. Debe, M. K., Schmoeckel, A. K., Vernstrom, G. D. & Atanasoski, R. High voltage stability of nanostructured thin film catalysts for PEM fuel cells. *J. Power Sources* **161**, 1002–1011 (2006).

36. Borup, R. *et al*. Scientific aspects of polymer electrolyte fuel cell durability and degradation. *Chem. Rev.* **107**, 3904–3951 (2007).

37. Genorio, B. *et al*. Tailoring the Selectivity and Stability of Chemically Modified Platinum Nanocatalysts to Design Highly Durable Anodes for PEM Fuel Cells. *Angew. Chem. Int. Ed.* **50**, 5468–5472 (2011).

38. Tang, W., Zhang, L. & Henkelman, G. Catalytic Activity of Pd/Cu Random Alloy Nanoparticles for Oxygen Reduction. *J. Phys. Chem. Lett.* **2**, 1328–1331 (2011).

39. Ho, V. T. T., Pan, C.-J., Rick, J., Su, W.-N. & Hwang, B.-J. Nanostructured $Ti_{0.7}Mo_{0.3}O_2$ Support Enhances Electron Transfer to Pt: High-Performance Catalyst for Oxygen Reduction Reaction. *J. Am. Chem. Soc.* **133**, 11716–11724 (2011).

40. Yoo, S. J. *et al*. Promoting effects of La for improved oxygen reduction activity and high stability of Pt on Pt–La alloy electrodes. *Energy Environ. Sci.* **5**, 7521–7525 (2012).

41. Rodriguez, J. A. & Goodman, D. W. The Nature of the Metal-Metal Bond in Bimetallic Surfaces. *Science* **257**, 897–903 (1992).

42. Wu, R. & Freeman, A. J. Bonding mechanism at bimetallic interfaces: Pd overlayer on various substrates. *Phys. Rev. B* **52**, 12419–12425 (1995).

Acknowledgements

Author contributions

S.J.H., S.-C.L. and S.-K.K. conceived the project and designed the experiments. S.J.H., S.J.Y., Y.-H.C. performed the experiments. S.J.H., S.J.Y. performed the EXAFS and XANES measurement and analysis. J.S. and S.-C.L. contributed to the calculation work. J.H.J., E.C., Y.-E.S., S.W.N., T.-H.L. analyzed the data. S.J.H., S.-C.L. and S.-K.K. co-wrote the paper. All authors discussed the results and commented on the manuscript.

Additional information

How to cite this article: Hwang, S.J. *et al*. Supported Core@Shell Electrocatalysts for Fuel Cells: Close Encounter with Reality. *Sci. Rep.* **3**, 1309; DOI:10.1038/srep01309 (2013).